Satellite retrieval of inherent optical properties in the turbid waters of the Yellow Sea and the East China Sea

Tingwei Cui (崔廷伟)[1*], Jie Zhang (张 杰)[1], Junwu Tang (唐军武)[2], Yi Ma (马 毅)[1], and Song Qing (青 松)[1]

[1]*First Institute of Oceanography, State Oceanic Administration, Qingdao 266061, China*

[2]*National Satellite Ocean Application Service, State Oceanic Administration, Beijing 100081, China*

[*]*E-mail: cuitingwei@fio.org.cn*

Received January 11, 2010

In situ-satellite match-ups of radiometric data are established in the turbid waters of the Yellow Sea and the East China Sea. Inherent optical properties (IOPs) are retrieved by match-up radiometric data and multi-band quasi-analytical algorithm (QAA). By comparing *in situ* spectra-retrieved IOPs with the satellite ones of moderate resolution imaging spectroradiometer (MODIS) and medium resolution imaging spectrometer (MERIS), the accuracy of satellite-derived IOPs is quantified. The median of the absolute percentage difference is found to be approximately 20% for the total absorption coefficient $a_{\rm t}(\lambda)$ at green and blue-green bands, and 30% for particulate material backscattering coefficient $b_{\rm bp}(\lambda)$ throughout the visible bands. The spatial pattern and temporal variability of IOPs along the eastern coast of China are clarified based on satellite images and the QAA model.

OCIS codes: 010.4450, 280.4788.

doi: 10.3788/COL20100808.0721.

Inherent optical properties (IOPs), including absorption coefficient, scattering phase function, and single scattering albedo[1], are considered inherent to seawater because they are determined only by the medium (seawater) itself, independent of the observation geometry and environmental conditions (e.g., illumination and wind speed). The spatial pattern and temporal variability of IOPs can provide important information about ocean properties and ocean color constituents[2−3].

IOP retrieval models can be divided into two categories: empirical and semi-analytical (SA). The empirical model, based on statistical regression[4−7], is easy to implement; however, it is limited to regional application. The SA model, with a clear theoretical foundation, represents the development trend. Most derivation of the SA models are analytical; however, a few empirical relationships are also involved and need be assessed for their applicability to specific waters. Typical SA models include the Carder algorithm[8], the Garver-Siegel-Maritorena (GSM) algorithm[9,10], and the quasi-analytical algorithm (QAA)[11].

The waters along the eastern coast of China are characterized by high turbidity. The accuracy of satellite-retrieved IOPs is still an open question. Part of the reason lies in the difficulty of obtaining a match-up dataset between *in situ* measurements and synchronous satellite observations. In this letter, the QAA model[12] is applied to satellite images of spectral normalized water-leaving radiance $L_{\rm wn}(\lambda)$ by moderate resolution imaging spectroradiometer (MODIS) and medium resolution imaging spectrometer (MERIS). The satellite-retrieved IOPs are compared with the *in situ* $L_{\rm wn}(\lambda)$-retrieved ones in the turbid coastal waters of the Yellow Sea (YS) and the East China Sea (ECS). The seasonal characteristics and the spatial distribution of IOPs along the coast of China are compared and assessed.

The Changjiang River pours a huge amount of fresh water and suspended particulate material (SPM) into the YS and ECS which are located on the continental shelf of the west bank of the Pacific Ocean. The seasonal variability of SPM and chlorophyll concentration, as well as transparency, are significant.

The coastal parts of YS and ECS are characterized by high turbidity. The particle backscattering coefficient $b_{\rm bp}(\lambda)$ at 532 nm in the study area spans three orders of magnitude from nearly 0.001 to 1.0 $\rm m^{-1}$[13]. The beam absorption coefficient $a_{\rm t}(\lambda)$ at 412 nm varies in the range of 0.1 and 10 $\rm m^{-1}$[6].

In situ optical data were acquired from the ocean optics experiment conducted in spring (March, April) and autumn (August, September) of 2003. These data are regarded as the most comprehensive, high-quality bio-optical observation results along the China Seas[14]. The dataset and the adopted measurement methodologies are described in detail by Tang *et al.*[14]. Spectral remote sensing reflectance $R_{\rm rs}(\lambda)$ ($\rm sr^{-1}$) is calculated by

$$R_{\rm rs}(\lambda) = (L_{\rm sw} - rL_{\rm sky})\rho_{\rm p}/L_{\rm p}\pi, \tag{1}$$

where $L_{\rm sw}$, $rL_{\rm sky}$, and $L_{\rm p}$ are the measured radiances of the ocean, reflected sky, and reference plank, respectively; and $\rho_{\rm p}$ is the known reflectance of the reference plank.

MERIS Level 2 (L2) data products of reduced resolution were collected from the European Space Agency (ESA) within the framework of the DRAGON project. MERIS water-leaving reflectance $\rho_{\rm w}(\lambda)$ was converted to remote sensing reflectance $R_{\rm rs}(\lambda)$ by

$$R_{\rm rs}(\lambda) = \rho_{\rm w}(\lambda)/\pi. \tag{2}$$

MODIS L2 and Level 3 (L3) products were downloaded from the National Aeronautics and Space Adminstration (NASA) Goddard Space Flight Center Distributed Active Archive Center (GSFC DAA). MODIS $L_{\rm wn}(\lambda)$ was

converted to $R_{\rm rs}(\lambda)$ by

$$R_{\rm rs}(\lambda) = L_{\rm wn}(\lambda)/F_{\rm o}(\lambda), \tag{3}$$

where $F_{\rm o}(\lambda)$ is the spectral mean extraterrestrial solar irradiance.

Under the QAA framework, the total absorption coefficients and particle backscattering coefficients were first retrieved. Subsequently, total absorption $a_{\rm t}(\lambda)$ ($\rm m^{-1}$) was decomposed into absorption by phytoplankton pigment $a_{\rm ph}(\lambda)$ ($\rm m^{-1}$), detritus, and colored dissolved organic matter (CDOM) $a_{\rm dg}(\lambda)$ ($\rm m^{-1}$). The basic equations of QAA are[12]

$$r_{\rm rs}(\lambda) = R_{\rm rs}(\lambda)/[0.52 + 1.7R_{\rm rs}(\lambda)], \tag{4}$$

$$u(\lambda) = \frac{-g_0 + [(g_0)^2 + 4g_1 r_{\rm rs}(\lambda)]^{1/2}}{2g_1}, \tag{5}$$

$$\begin{cases} \chi = lg\left(\dfrac{r_{\rm rs}(443) + r_{\rm rs}(490)}{r_{\rm rs}(555) + 5\frac{r_{\rm rs}(667)}{r_{\rm rs}(490)} r_{\rm rs}(667)}\right) \\ a_{\rm t}(555) = a_{\rm w}(555) + 10^{(-1.146 - 1.366\chi - 0.469\chi^2)} \end{cases}, \tag{6}$$

$$b_{\rm b}(555) = \frac{u(555)a_{\rm t}(555)}{1 - u(555)}, \tag{7}$$

$$Y = 2.0\left\{1 - 1.2\exp\left[-0.9\frac{r_{\rm rs}(443)}{r_{\rm rs}(555)}\right]\right\}, \tag{8}$$

$$\begin{aligned} b_{\rm bp}(\lambda) &= b_{\rm bp}(555)\left(\frac{555}{\lambda}\right)^Y \\ &= [b_{\rm b}(555) - b_{\rm bw}(555)]\left(\frac{555}{\lambda}\right)^Y, \end{aligned} \tag{9}$$

$$\begin{cases} \alpha = \exp\left[(S(440 - 410)\right] \\ \beta = 0.71 + \dfrac{0.06}{0.8 + r_{\rm rs}(440)/r_{\rm rs}(555)} \end{cases}, \tag{10}$$

$$\begin{cases} a_{\rm dg}(440) = \dfrac{[a(410) - \beta a(440)] - [a_{\rm w}(410) - \beta a_{\rm w}(440)]}{\alpha - \beta} \\ a_{\rm ph}(440) = a_{\rm t}(440) - a_{\rm w}(440) - a_{\rm dg}(440) \end{cases}, \tag{11}$$

$$\begin{cases} a_{\rm dg}(\lambda) = a_{\rm dg}(440)\exp\left[S(440 - \lambda)\right] \\ a_{\rm ph}(\lambda) = a_{\rm t}(\lambda) - a_{\rm w}(\lambda) - a_{\rm dg}(440)\ \exp\left[S(440 - \lambda)\right] \end{cases}, \tag{12}$$

where $r_{\rm rs}$ ($\rm sr^{-1}$) denotes the remote sensing reflectance just below the sea surface; $b_{\rm b}$ ($\rm m^{-1}$) denotes the total backscattering coefficient of the sea water; $a_{\rm w}$ ($\rm m^{-1}$) denotes the absorption coefficient of pure sea water; $b_{\rm bp}$ ($\rm m^{-1}$) denotes the backscattering coefficient of particulate material; $b_{\rm bw}$ ($\rm m^{-1}$) denotes backscattering coefficient of pure sea; U denotes the ratio of $b_{\rm b}$ to $(a + b_{\rm b})$; G_0 denotes the parameter relating $r_{\rm rs}$ and u and equals to 0.0895; G_1 denotes the parameter relating $r_{\rm rs}$ and u and equals to 0.1247; χ denotes the empirical parameter used in $a_{\rm t}(555)$ computation; Y denotes the power exponent of $b_{\rm bp}(\lambda)$; α and β denote the empirical parameters used in $a_{\rm t}(\lambda)$ decomposition; $S(\rm nm^{-1})$ denotes the power exponent of $a_{\rm dg}(\lambda)$, which equals 0.014. Figure 1 provides the flowchart of the algorithm[11].

A match-up dataset between satellite and *in situ* $R_{\rm rs}(\lambda)$ was established through the following five steps:

1) Select the satellite L2 products acquired on the day of *in situ* observation. Extract products of the pixels centered on the *in situ* location based on 3×3 pixel boxes.

2) For each box, eliminate invalid satellite pixels that have negative or overflow values of $R_{\rm rs}(\lambda)$.

3) Calculate the median and standard deviation (SD) of $R_{\rm rs}(\lambda)$. Delete the outlier pixels from every pixel box to prevent abnormal values from influencing statistical results. Outliers are identified as pixels whose values are larger than 1.5 times SD[15]. The process is implemented separately for different bands.

4) Check the percentage of good pixels in the box. If the number of good pixels is not less than 4, the pixel box is adopted for the following match-up analysis.

5) The median of the remaining pixels is compared with the corresponding *in situ* measurements.

For all the valid match-ups, the intervals between satellite overpass and *in situ* measurements were less than 6 h. Figure 2 shows the spatial distribution of the valid match-ups for MERIS and MODIS. It should be emphasized that the two match-up datasets for MERIS and MODIS were different, and only less than a half of all the match-ups were identical.

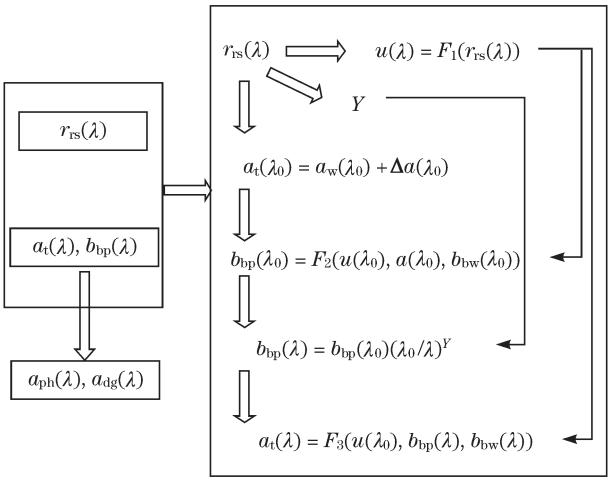

Fig. 1. Flowchart of the QAA model[11].

Statistical parameters for the assessment include median of absolute percentage difference $\rm APD_m$ (i.e., the median value of the ensemble $(|y_i - x_i|x_i)_{i=1,N}$, where y_i is the satellite-retrieved value, x_i is the *in situ* value, N is the number of match-up datasets), root mean square error (RMS), the median (Ra.) and the semi-interquartile range (SIQR) of satellite to *in situ* ratio[15]. RMS and SIQR are calculated as

$$\rm RMS = \sqrt{\frac{\sum_{i=1}^{N}(y_i - x_i)^2}{N}}, \tag{13}$$

$$\rm SIQR = \frac{(Q_3 - Q_1)}{2}, \tag{14}$$

where Q_3 and Q_1 are the third and first quartiles. Determination coefficient (R^2), and slope and intercept for linear regression are given. All the statistics are calculated in linear scale.

Comparisons between *in situ* and satellite-derived $R_{\rm rs}(\lambda)$ at four bands (443, 490, 555, and 670 nm) involved

Table 1. Comparison of Satellite and *In Situ* R_{rs} (λ)

		Ra. (SIQR)	APD_m(%)	RMS* (sr^{-1})	R^2	Slope	Intercept	N
MERIS	$R_{rs}(443)$	1.501 (0.461)	50	0.0036	0.732	1.051	0.002	20
	$R_{rs}(490)$	1.248 (0.247)	25	0.0020	0.914	0.894	0.002	20
	$R_{rs}(555)$	1.027 (0.129)	15	0.0016	0.975	0.878	0.001	20
	$R_{rs}(670)$	1.049 (0.477)	27	0.0014	0.902	0.992	0.000	20
MODIS	$R_{rs}(443)$	1.012 (0.251)	25	0.0025	0.790	0.886	0.001	22
	$R_{rs}(490)$	0.948 (0.151)	17	0.0027	0.872	0.838	0.001	22
	$R_{rs}(555)$	0.849 (0.160)	21	0.0038	0.903	0.782	0.001	22
	$R_{rs}(670)$	0.870 (0.124)	18	0.0025	0.846	0.846	0.000	19

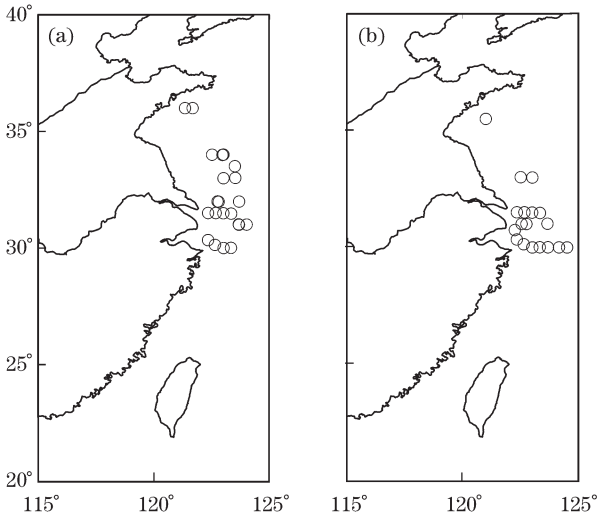

Fig. 2. Spatial distribution of the valid (a) MERIS and (b) MODIS match-ups for 3×3 pixel boxes.

in the QAA retrieval are shown in Table 1. MERIS $R_{rs}(\lambda)$ tends to overestimate the *in situ* data by 15%–50%, and the best retrieval is obtained at 555 nm. The APD_m of MODIS $R_{rs}(\lambda)$ is 17%–25%, with the best retrieval at 490 nm.

QAA-based comparisons between satellite and *in situ* retrieved IOPs are given in Fig. 3. Corresponding statistics are shown in Table 2.

MERIS $R_{rs}(\lambda)$ retrieved $a_t(\lambda)$ underestimates the *in situ* retrievals, with an APD_m of 20%–50% and RMS of 0.031–0.630 m^{-1}. At bands except 670 nm, the MERIS and *in situ* $a_t(\lambda)$ retrievals have significant correlations ($R^2 > 0.7$; $p < 0.01$), and the linear regression have slopes of 0.741–0.895 and intercepts of approximately 0. The best agreement between MERIS and *in situ* retrievals is achieved at green bands of 555 nm, followed by blue-green bands of 490 nm. The significant reduction in the agreement in the blue bands can be explained by the error transfer and accumulation during the extrapolation from retrievals at the reference band (555 nm) by the SA algorithm. MODIS and *in situ* retrievals of total absorption coefficient have an APD_m of 11%–27% and a RMS of 0.024–0.237 m^{-1}. The linear regression reveals slopes of 0.542–0.861, intercepts of less than 0.1, and determination coefficients R^2 larger than 0.5 (except at 670 nm). The retrievals among bands are more balanced than those of MERIS, and the best performances are obtained

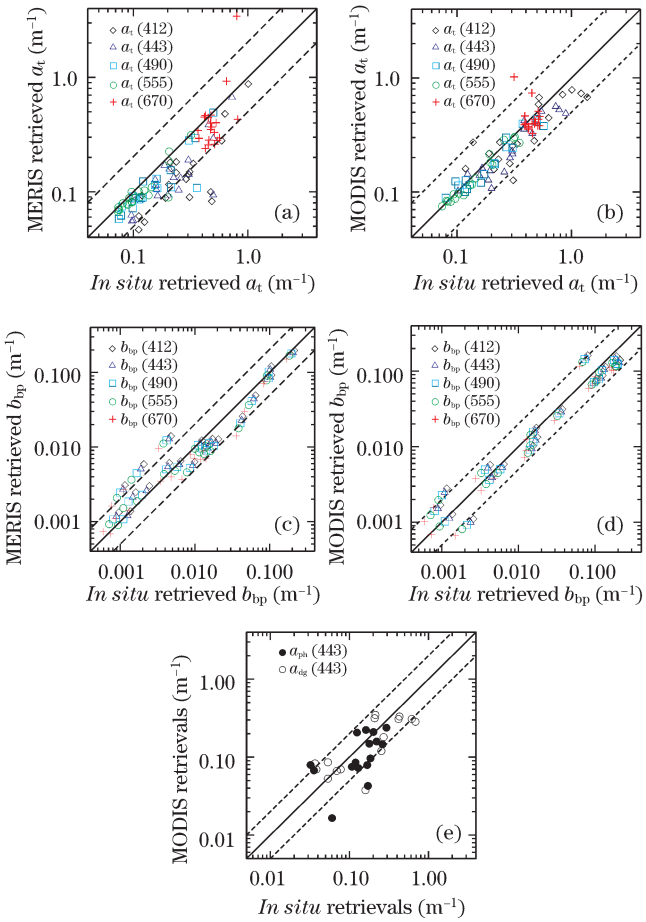

Fig. 3. QAA-based comparison between satellite and *in situ* retrieved IOPs. (a) MERIS $a_t(\lambda)$; (b) MODIS $a_t(\lambda)$; (c) MERIS $b_{bp}(\lambda)$; (d) MODIS $b_{bp}(\lambda)$; (e) $a_{ph}(\lambda)$ and $a_{dg}(\lambda)$.

at bands of 555 and 490 nm. To summarize, MODIS and MERIS retrieved $a_t(\lambda)$ at bands of 555 and 490 nm are in agreement with the *in situ* retrievals, with an APD_m of approximately 20% and a RMS of 0.024–0.069 m^{-1}. In addition, the different match-up datasets and the atmospheric correction methods may account for the difference between MERIS and MODIS assessment results.

The comparison of MERIS and *in situ* retrieved $b_{bp}(\lambda)$ indicates an APD_m of less than 30% and a RMS of about 0.01 m^{-1}. Significant correlations are observed for these retrievals ($R^2 > 0.97$; $p < 0.01$), with the slopes and inter-

Table 2. Comparison of Satellite and *In Situ* Retrieved IOPs

		Ra. (SIQR)	APD_m(%)	RMS (m^{-1})	R^2	Slope	Intercept	N
MERIS	$a_t(412)$	0.504 (0.152)	50	0.183	0.757	0.746	−0.061	20
	$a_t(443)$	0.623 (0.118)	38	0.129	0.716	0.741	−0.024	20
	$a_t(490)$	0.784 (0.071)	22	0.069	0.777	0.800	−0.006	20
	$a_t(555)$	0.909 (0.067)	20	0.031	0.828	0.895	−0.003	20
	$a_t(670)$	0.761 (0.206)	31	0.630	0.380	3.556	−1.278	20
MODIS	$a_t(412)$	0.808 (0.252)	27	0.237	0.745	0.542	0.120	18
	$a_t(443)$	0.857 (0.193)	27	0.157	0.572	0.504	0.129	22
	$a_t(490)$	0.905 (0.141)	16	0.057	0.906	0.722	0.043	22
	$a_t(555)$	0.948 (0.095)	11	0.024	0.935	0.861	0.015	22
	$a_t(670)$	0.872 (0.078)	15	0.222	0.012	−0.374	0.657	19
MERIS	$b_{bp}(412)$	0.997 (0.301)	28	0.009	0.976	0.933	−0.001	20
	$b_{bp}(443)$	0.979 (0.283)	28	0.009	0.979	0.926	−0.001	20
	$b_{bp}(490)$	0.952 (0.258)	27	0.008	0.981	0.916	−0.001	20
	$b_{bp}(555)$	0.932 (0.229)	29	0.008	0.983	0.904	−0.001	20
	$b_{bp}(670)$	0.901 (0.214)	28	0.008	0.982	0.886	−0.002	20
MODIS	$b_{bp}(412)$	0.828 (0.169)	32	0.032	0.852	0.738	0.005	22
	$b_{bp}(443)$	0.831 (0.158)	31	0.031	0.853	0.729	0.005	22
	$b_{bp}(490)$	0.825 (0.141)	28	0.030	0.853	0.719	0.005	22
	$b_{bp}(555)$	0.831 (0.154)	28	0.029	0.854	0.705	0.005	22
	$b_{bp}(670)$	0.798 (0.217)	29	0.027	0.854	0.680	0.004	22
MODIS	$a_{ph}(443)$	0.716 (0.290)	44	0.071	0.386	0.580	0.033	16
	$a_{dg}(443)$	0.928 (0.449)	50	0.148	0.534	0.415	0.082	18

cepts of the linear regression larger than 0.88 and near 0, respectively. The statistics of the comparison have little spectral variability. The APD_m and RMS between the MODIS and *in situ* retrieved $b_{bp}(\lambda)$ are approximately 30% and 0.03 m^{-1}, respectively. Significant linear correlation is also found ($R^2 > 0.85$, $p < 0.01$, slope > 0.68, intercept < 0.005). Similar statistics are obtained for the major ocean color bands.

The retrieval accuracy of $a_{ph}(\lambda)$ and $a_{dg}(\lambda)$ by QAA model is mainly dependent on the retrieval uncertainty of $a_t(\lambda)$ in the blue bands. The *in situ* retrievals are in better agreement (∼30%) with MODIS-retrieved $a_t(\lambda)$ than with those obtained with MERIS, especially in shorter bands; hence, only MODIS-retrieved $a_{ph}(\lambda)$ and $a_{dg}(\lambda)$ are compared with *in situ* retrievals. Table 2 and Fig. 3 show the comparison results at 443 nm. The APD_m of the MODIS and *in situ* retrieved $a_{ph}(443)$ is 44% and that for $a_{dg}(443)$ is 50%. Most of the disagreement may be attributed to the difference between *in situ* and satellite retrieved $a_t(\lambda)$.

Figure 4 shows the satellite retrievals of $b_{bp}(555)$ and $a_t(555)$ along the coast of China by QAA model and MODIS L3 season-averaged products.

Figures 4(a)–(d) show that the general pattern of $b_{bp}(555)$ in the YS is characterized by high values along the coast and low values at the middle part. In winter, water with low $b_{bp}(555)$ ($<\sim 0.05$ m^{-1}) is mainly located in the middle eastern part of South YS and in the northeastern part of North YS. Among the four seasons, the magnitude of regionally averaged $b_{bp}(555)$ in winter is the highest. In spring, the area of the region with low values of particle backscattering increases significantly compared with that in winter, and low $b_{bp}(555)$ waters in the YS are connected with those in the ECS near the southern part of the Korean Peninsula. In summer, majority of the YS is dominated by water with low $b_{bp}(555)$, and the regionally averaged value is at the yearly minimum. The spatial pattern is uniform throughout South and North YS. In autumn, although the majority of the YS exhibits the feature of low $b_{bp}(555)$, the increasing trend of $b_{bp}(555)$ in the offshore parts is evident.

SPM contributes to the majority of backscattering signal; hence, the spatial distribution of $b_{bp}(555)$ reflects the SPM pattern. The foregoing seasonal characteristics of $b_{bp}(555)$ are consistent with that of SPM[16,17].

For ECS, as indicated in Fig. 4, SPM from the Changjiang River spreads farthest from the coast of China during autumn and spring, although the seasonal transportation of freshwater and SPM is largest in summer. Moreover, the direction of SPM plume in summer is nearly directly eastwards. In autumn and winter, the direction is southeastern.

In the Bohai Sea, $b_{bp}(555)$ in autumn and winter is higher than in summer and spring, which can be attributed to SPM re-suspension with the perturbation triggered by strong winds. Moreover, the seasonal variability is also consistent with that of the SPM described by Cui *et al.*[18]

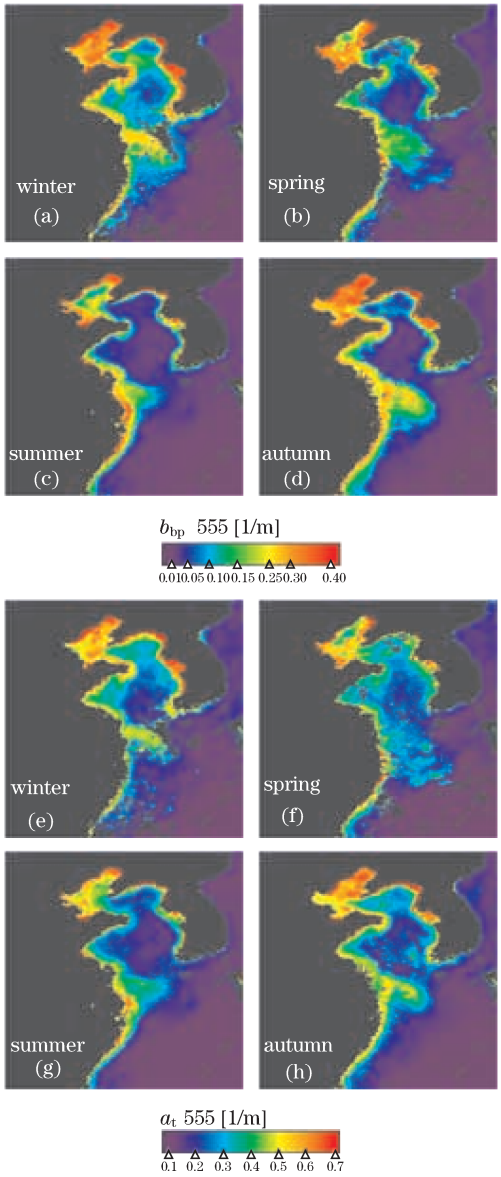

Fig. 4. Satellite retrieved (a)–(d) $b_{bp}(555)$ and (e)–(h) $a_t(555)$ pattern by QAA model, and MODIS L3 seasonally averaged data in 2008.

The spatial pattern, as well as the seasonal variation of $a_t(555)$ along the coast of China, is similar with that of $b_{bp}(555)$.

In conclusion, the satellite and *in situ* retrievals of IOPs in the YS and ECS are compared in this letter. Through the comparison, the accuracy of satellite derived IOPs is quantified. The median of the absolute percentage difference is approximately 20% for the total absorption coefficient $a_t(\lambda)$ at green and blue-green bands, and 30% for particulate material backscattering coefficient $b_{bp}(\lambda)$ throughout the visible bands. With specific uncertainties, the results indicate the potential and feasibility of elucidating the spatiotemporal variation of IOPs in turbid waters based on satellite images. The spatial pattern and temporal variability of IOPs along the coast of China are analyzed using satellite images and the SA model.

This work was supported by the National Natural Science Foundation of China (Nos. 40706060 and 60802089), the High-Tech Research and Development Program of China (Nos. 2007AA092102 and 2007AA12Z161), and the State Oceanic Administration (SOA) of China (Nos. 200705027, 200805011, and 2008401). We would like to thank NASA and ESA for the distribution of MODIS and MERIS data.

References

1. C. D. Mobley, *Light and Water*: *Radiative Transfer in Natural Waters* (Academic Press, New York, 1994).
2. T. Cui, J. Zhang, Y. Ma, L. Sun, and W. Zhao, Acta Opt. Sin. (in Chinese) **28,** 2041 (2008).
3. W. Zhou, W. Cao, C. Li, Z. Sun, G. Wang, and J. Zhao, Acta Opt. Sin. (in Chinese) **28,** 1429 (2008).
4. Z. P. Lee, K. L. Carder, T. G. Peacock, C. O. Davis, and J. L. Mueller, Appl. Opt. **35,** 453 (1996).
5. Z. P. Lee, K. L. Carder, R. G. Steward, T. G. Peacock, C. O. Davis, and J. S. Patch, J. Geophys. Res. **103,** 27967 (1998).
6. X. Wang, J. Tang, Q. Song, and C. Ma, Oceanologia Et Limnologia Sinica (in Chinese) **37,** 256 (2006).
7. T. Li, Q. Chen, A. Yang, and D. Bi, Ocean Technology (in Chinese) **23,** (3) 10 (2004).
8. K. L. Carder, F. R. Chen, Z. P. Lee, S. K. Hawes, and D. Kamykowski, J. Geophys. Res. **104,** 5403 (1999).
9. S. Maritorena, D. A. Siegel, and A. R. Peterson, Appl. Opt. **41,** 2705 (2002).
10. S. A. Garver and D. A. Siegel, J. Geophys. Res. **102,** 18607 (1997).
11. Z. P. Lee, K. L. Carder, and R. A. Arnone, Appl. Opt. **41,** 5755 (2002).
12. Z. Lee, B. Lubac, J. Werdell, and R. Arnone, "An update of the quasi-analytical algorithm (QAA_v5)" http://www.ioccg.org/groups/software_OCA/QAA_v5.pdf (May 11, 2009).
13. Q. Song and J. Tang, Acta Oceanologica Sinica (in Chinese) **28,** (4) 56 (2006).
14. J. Tang, X. Wang, Q. Song, T. Li, H. Huang, J. Ren, and W. Jian, Advances in Marine Science (in Chinese) **22,** (suppl.) 1 (2004).
15. S. W. Bailey and P. J. Werdell, Remote Sensing of Environment **102,** 12 (2006).
16. Z. Yang, Z. Guo, Z. Wang, J. Xu, and W. Gao, Acta Oceanologica Sinica (in Chinese) **14,** (2) 81 (1992).
17. W. Wang and W. Jiang, J. Ocean Univ. China **7,** 385 (2008).
18. T. Cui, J. Zhang, Y. Ma, W. Zhao, and L. Sun, Acta Oceanologica Sinica (in Chinese) **31,** (5) 10 (2009).